Electronic Supporting Information

Collagen fibers-reinforced, tough and adaptive conductive organohydrogel e-skin for multimodal sensing applications

Zhen He[a,b], Jialu Shen[a,b], Maohua Lan[a,b], Haibin Gu[a,b,*]

[a] Key Laboratory of Leather Chemistry and Engineering of Ministry of Education, Sichuan University, Chengdu 610065, China.

[b] National Engineering Laboratory for Clean Technology of Leather Manufacture, Sichuan University, Chengdu 610065, China.

Corresponding author: Haibin Gu, e-mail: guhaibinkong@126.com, orcid.org/0000-0003-0342-360X.

Experimental Section

Materials

Polyvinyl alcohol (PVA, degree of hydrolysis: 95.5-96.5%, molecular weight: 85000-124000 Da), Silver nitrate and Gelatin (Gel) were provided from Chron Chemicals Co., Ltd. (Chengdu, China). Tara tannin and buffing dust (BD) were purchased from Ting Jiang New Materials Co., Ltd. (Chengdu, China)

Characterization Instruments

UV–vis spectra were recorded by using a UV–vis spectrophotometer (UV1900, Shanghai Jinghua Technology Co., Ltd.). The infrared (IR) spectra with wavelength range of 500 – 4000 cm^{-1} were analyzed by Fourier Transform infrared (FTIR) spectrometer (Nicolet is 10, Thermo Fisher Scientific, USA). X-ray photoelectron spectroscopy (XPS) experiments were performed on binding energies of different elements (C 1s, N 1s, O 1s) by using ESCALAB Xi+ (Thermo Scientific, USA). The micromorphology of hydrogel was characterized by using a SM-7500 field emission scanning

electron microscope (SEM, JEOL, Japan). The morphology BD-CQDs and BD-BD-CQDs@AgNPs were determined by using transmission electron microscopy (TEM) and high magnification transmission electron microscopy (HRTEM) (JEM-F200, Japan). The dynamic light scattering (DLS, Zetasizer nano zip, Britain) were used to analyze the particle sizes and hydraulic diameters of BD-CQDs@AgNPs.

Mechanical Property Test of Hydrogels

A universal tensile machine (INSTRON5967, USA) was used to determine the mechanical property of the hydrogel sample. The hydrogel was made into a rectangular sample (40 mm × 6 mm × 2 mm). Then, the sample was stretched at a speed of 100 mm/min to obtain the stress-strain curve of the hydrogel.

The strain (ε, %) was calculated as follows:

$$\varepsilon = \frac{l - l_0}{l_0} \times 100$$

where l and l_0 represent the real-time and the original lengths of the test spline, respectively.

The stress (σ, MPa) was calculated as follows:

$$\sigma = \frac{F}{S}$$

where F indicates the load (N), *S* represents the cross-sectional area of the test spline (mm^2).

Anti-freezing and Moisturizing Test of Hydrogels

The freezing point of the BPGC hydrogel and the BPGC-Gly organohydrogel were determined using differential calorimetry scanning (DCS 214, NETZSCH, Germany). The test temperature range was -60 °C to 20 °C, and the temperature change rate was 5 °C/min.

The BPGC hydrogel and the BPGC-Gly organic hydrogel were placed in an environment with a temperature of 25 °C and relative humidity (RH) of 60%. Then, the mass of the hydrogels with time was recorded. The weight ratio (WR) of the hydrogels at different times was evaluated by the following formula：

$$WR(\%) = \frac{W_t}{W_0} \times 100\%$$

where W_0 (g) is the mass of the original hydrogel and W_t (g) is the mass of the hydrogel at different times.

Antibacterial Test of Hydrogels

Gram-negative (*Escherichia coli*, *E. coli*, ATCC25922) and Gram-positive (*Staphylococcus aureus*, *S. aureus*, ATCC6538) bacteria were used as test strains. The antibacterial experiments of hydrogels were preformed using the classical disc diffusion method. Specifically, the mother liquor of *S. aureus* (or *E. coli*) was transferred to the freshly prepared and sterilized Luria-Bertani (LB) broth nutrient solution, and cultured at 37 °C for 24 h. Then, the activated *S. aureus* (or *E. coli*) was inoculated onto the sterilized and cooled agar petri dish plate. Finally, the hydrogel discs were covered on the fixed area of the plate, and the plate was transferred to an incubator with constant temperature (37°C) and humidity (60%RH) for culture, then the results of the inhibition zone were observed and recorded after 24 h.

Cytotoxicity Test of BPGC-Gly

The cytotoxicity of BPGC-Gly was determined using the 2-(2-methoxy-4-nitrophenyl)-3-(4-nitrophenyl)-5-(2,4-disulfonic acid benzene)-2h-tetrazolium monosodium salt (CCK-8) method. L929 cells at logarithmic growth stage were inoculated into 96-well plates at a density of 5,000 cells per well. Subsequently, these cells were cultured for 24 h with different concentrations of BPGC-Gly extract (0.01, 0.2, 0.4, 0.6, 0.8 and 1.0 mg/mL, respectively). After that, the medium was removed, and each well was thoroughly cleaned with PBS (phosphate buffer saline, pH 7.4) twice. 100 μL of medium containing 10% CCK-8 and 5% CO_2 was added and cultured for 2 h in an incubator at 37°C. Finally, the absorbance at 450 nm was measured by a microplate reader.

Electrical Property of BPGC-Gly

The conductivity and strain/compression sensing property of BPGC-Gly were tested using an electrochemical workstation (i-t curve mode, CHI660E, Shanghai Chenhua Instrument Co., Ltd.). For the electrical performance tests, BPGC-Gly was made into rectangular shapes with a size of 40 mm (length) × 10 mm (width) × 1 mm (thickness). The conductivity (σ, S/m) and relative resistance changes (ΔR/R0 (%)) of BPGC-Gly were calculated according to the following formulas:

$$\sigma = \frac{L}{R \times A}$$

where the L is the distance between two adjacent probes (m), R represents the resistance of BPGC-Gly (Ω), and A indicates the cross-sectional area (m^2).

$$\frac{\Delta R}{R_0}(\%) = \frac{(R - R_0)}{R_0} \times 100$$

where R_0 and R are the resistance without and with applied strain, respectively. During the electrical tests, the voltage is set to 5 V.

The electrical property of BPGC-Gly was also evaluated by using the gauge factor (GF), its calculation method was reported in the literature, and the known formular is as follows:

$$GF = \frac{(R - R_0)/R_0}{\varepsilon}$$

where ε represents the tensile strain (%) of BPGC-Gly.

BPGC-Gly was made into cylinder shapes with dimensions of 15 mm (diameter) × 10 mm (thickness). The conductivity (σ, S/m) and relative resistance changes (ΔR/R0 (%)) of BPGC-Gly were calculated according to the following formulas:

Pressure sensitivity (*S*) reflects the influence of pressure on changes in the relative resistance of the pressure sensor.

$$S = \frac{|\Delta R|/R_0}{P}$$

Where P stands for pressure (kPa).

Sensing Test of BPGC-Gly Sensor

The electrical conductivity was determined using an electrochemical workstation (CHI760E, Chenhua, China). The sensing property of BPGC-Gly was tested by various monitoring modes (temperature/humidity sensing, strain/pressure-resistance response, and bioelectric signal). Firstly, BPGC-Gly sample (length: 40 mm, width: 10 mm, thickness: 1 mm) was sealed using 3M tape and then connected to the electrochemical workstation, the relative conductance ($\Delta G/G_0$) changes in response to different temperatures and humidity were monitored at 1.5 V. Secondly, BPGC-Gly was made into rectangular shapes with a size of 40 mm (length) × 10 mm (width) × 1 mm (thickness) and applied to the surface of human skin with transparent tape. When the volunteer completed a series of actions (such as frowning, swallowing, finger bending, etc.), the changes of electric current in real time were record by the electrochemical workstation. According to these data, the real-time $\Delta R/R_0$ of different movements can be calculated and signal curve of $\Delta R/R_0$ vs time can be drawn for the analysis of the monitoring results. Thirdly, BPGC-Gly samples (15 mm × 15 mm × 10 mm) were prepared as a 4 × 4 array of pressure sensors to be used in

conjunction with an electrochemical workstation to monitor the pressure distribution of the weight. Finally, three slices of BPGC-Gly (10 mm × 10 mm × 1 mm) were connected to a customized multi-channel voltage collection device through wires (red, green, and yellow) as positive, ground, and reference electrodes, respectively. Three prepared electrodes were directly attached to different parts (arm, thigh, face, chest and so on) of the volunteer's body. Then, the collected and recorded data were wirelessly transmitted to the computer through the Bluetooth module (baud rate 115200).

Preparation and characterization of BD-CQDs and BD-CQDs@AgNPs

We initially analyzed the microstructure and physicochemical properties of BD-CQDs. As depicted in Fig. S5b-d, the microstructure of BD-CQDs was observed by TEM and HRTEM. The BD-CQDs presented uniformly dispersed spherical particles with an average particle size of 5.25 nm. And the lattice fringes of 0.213 nm could be observed by HRTEM image, which corresponded to the graphene C (100) plane.[S1] These results proved the successful synthesis of BD-CQDs. As illustrated in Fig. S5e, the UV-vis spectra of BD-CQDs showed two obvious photo absorption peaks near 205 nm and 275 nm, belonging to the π-π* electron transition of the C=C double bond and the n-π* electron transition of the C=N/C=O bond, respectively.[S2] In addition, according to the photoluminescent emission spectrum (red line) and photoluminescent excitation spectrum (blue line), the optimal emission wavelength of 475 nm could be obtained when BD-CQDs was excited at 400 nm. As shown in the inset of Fig. S5e, the BD-CQDs solution was yellow and transparent under daylight, and exhibited a blue fluorescence under UV lamps of 365 nm, which was consistent with the emission spectroscopy results.

The composition and structure of BD-CQDs were further analyzed by Fourier transform infrared (FTIR) and X-ray photoelectron spectrometer (XPS). As shown in the Fig. S5f, Tara tannin has distinct characteristic vibration peaks at 1721 cm^{-1} and 1613 cm^{-1}, respectively, attributed to the stretching vibrations of the C=C and C=O double bonds in the benzene ring.[S3] Similarly, the stretching vibration peaks of the amide I band (C=O) and the amide II band (N-H) could be observed at 1640 cm^{-1} and 1540 cm^{-1} respectively in the FTIR of BD.[S4] Notably, the absorption peak of BD-

CQDs became significantly stronger in the range of 1664-1340 cm^{-1}, which was due to the isomerization of various characteristic groups during the hydrothermal reaction, resulting in a surge in the number of C=C double bond structures.[S5] Meanwhile, all three samples displayed broad absorption peaks in the range of 3200-3600 cm^{-1}, which is attributed to the telescopic vibration peaks of hydroxyl and amino groups, proving that the N- and O-containing functional groups in Tara tannin and BD were introduced into BD-CQDs, which would be favorable to the improvement of the reactivity of BD-CQDs.[S6] The elemental composition of BD-CQDs was further explored using XPS. The full spectrum diagram presented in Fig. S5g showed that the BD-CQDs was mainly composed of C (62.66%), N (11.40%) and O (25.93%) elements. The high-resolution spectra of the three elements (C, N, and O) were also analyzed to investigate the detailed functional group composition of BD-CQDs. As illustrated in the Fig. S5h, the C 1s spectrum of the BD-CQDs exhibited three different peaks at 288.04, 285.87 and 284.53 eV, corresponding to the C=C/C-C, C-O/ C-N and C=O bonds respectively, demonstrating that BD-CQDs may contain the active groups (amino, carboxyl and hydroxyl) of Tara tannin and BD.[S7] As depicted in Fig. S5i, the N 1s high-resolution spectra could be deconvolved to 401.14 eV (C-NH_2) and 399.56 eV (C-N-C), which further proved that the N element in BD was successfully doped into BD-CQDs.[S8] In addition, C=O double bond with a binding energy of 531.8 3 eV as well as C-O bond with a binding energy of 530.84 eV could be observed by O 1s high-resolution spectra, and these results were consistent with the infrared spectra (Fig. S5j). Therefore, we believed that the phenolic hydroxyl group in Tara tannin in the precursor and the amino group, carboxyl group and hydroxyl group in BD were successfully introduced to the surface of BD-CQDs, which was conducive to the enhancement of the water-solubility, electrical conductivity and stability of BD-CQDs.

Based on the above research, we concluded that BD-CQDs prepared from BD and Tara tannin could be used as reducing agent and stabilizing agent for the synthesis of AgNPs due to the large amount of phenolic hydroxyl and active groups (Fig. S6). Typically, $AgNO_3$ were reduced to AgNPs by the phenol hydroxyl groups and amino groups on BD-CQDs, while the catechol groups were oxidized to hemiquinone/quinone.[S9] As illustrated in Fig. S1 and S3, the reduced BD-CQDs@AgNPs solutions under different conditions presented different color changes of light yellow, dark yellow and brown yellow. As depicted in Fig. S2a and S4a, the redox reaction between silver nitrate and BD-CQDs could be confirmed by observing surface plasmon resonance (SPR) in the range of 410 –

450 nm of BD-CQDs@AgNPs using ultraviolet-visible (UV-Vis) spectroscopy.[S10] The hydrated particle size and stability of AgNPs that prepared under different pH (6-10) and different $AgNO_3$ concentration (0.015M – 0.070M) were analyzed using dynamic light scattering (DLS) and Zeta potential (ZP). Generally, the smaller PDI means the better solution dispersion. As shown in Fig. S2, S4 Table S1 and S2, the minimum hydrated particle size (24.41 nm) and PDI (0.277) of AgNPs were appeared at the condition of pH=8 and $AgNO_3$ concentration of 0.06M. In addition, the stability of AgNPs was evaluated by the absolute value of Zeta potential. The greater the absolute value, the more stable the solution. [S11] As described in Table S1 and S2, the Zeta potential of sample NO.4 (NO.9) could up to -39.2 mV, indicating that it has good stability. Therefore, according to the experiments results of DLS and Zeta potential, the NO.9 sample (pH = 8, $AgNO_3$ concentration of 0.06M) was selected for subsequent experiments (NO.9 sample was named as BD-CQDs@AgNPs).

The valence state of Ag elements in BD-CQDs@AgNPs was analyzed by XPS. As shown in Fig. S5k, the characteristic binding energy of Ag ($3d_{5/2}$) and Ag ($3d_{3/2}$) peaks were observed at 367.18 and 373.18 eV respectively, which clearly demonstrate the presence of metallic silver, indicating the successful reduction of AgNPs by BD-CQDs.[S12] The microstructure of BD-CQDs@AgNPs was further examined by using Transmission Electron Microscopy (TEM) and High-Resolution Transmission Electron Microscopy (HRTEM). As could be seen from Fig. S5l, the shape of BD-CQDs@AgNPs was spherical with an average particle size of 3.8 nm. Notably, the average particle size of BD-CQDs@AgNPs obtained by TEM (3.80 nm) was much smaller than the hydrated particle size (24.41 nm) measured by DLS (Fig. S5m). This is due to the fact that the surface of AgNPs is negatively charged (ZP = -39.2 mV), which tends to form electrostatic interaction with positively charged ions in solution, so as to form a stable supramolecular layer on the surface of AgNPs. It is precisely because of the existence of this supramolecular layer that the hydration particle size of AgNPs in DLS test is much larger than that in TEM test (TEM only showed the particle size of dried AgNPs). Meanwhile, the BD-CQDs could be used as stabilizer to gather on the surface of AgNPs, maintaining the distance between the adjacent AgNPs and preventing their agglomeration. In addition, the HR-TEM image of BD-CQDs@AgNPs clearly revealed a lattice spacing of 0.35 nm, corresponding to the (111) crystal plane of AgNPs (Fig. S5n).[S13] All these results strongly confirm the role of BD-CQDs in the reduction and stabilization of AgNPs. In addition, the conductivity of BD-CQDs@AgNPs was evaluated by a conductivity meter. As shown in the Fig. S5o, the

conductivity of the prepared BD-CQDs could reach 0.71 S/m compared with deionized (DI) water (0 S/m), and the conductivity of BD-CQDs@AgNPs could reach 0.84 S/m. Simultaneously, the BD-CQDs@AgNPs could successfully light up the LEDs, indicating that both BD-CQDs and BD-CQDs@AgNPs have good electrical conductivity (Fig. S5p).

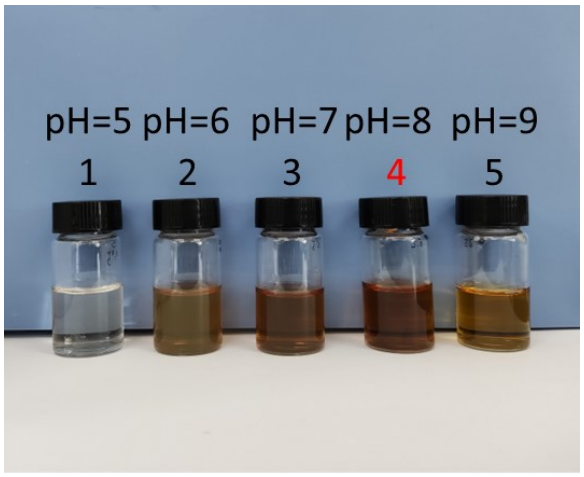

Fig. S1 Photos of BD-CQDs@AgNPs solutions prepared under different pH conditions.

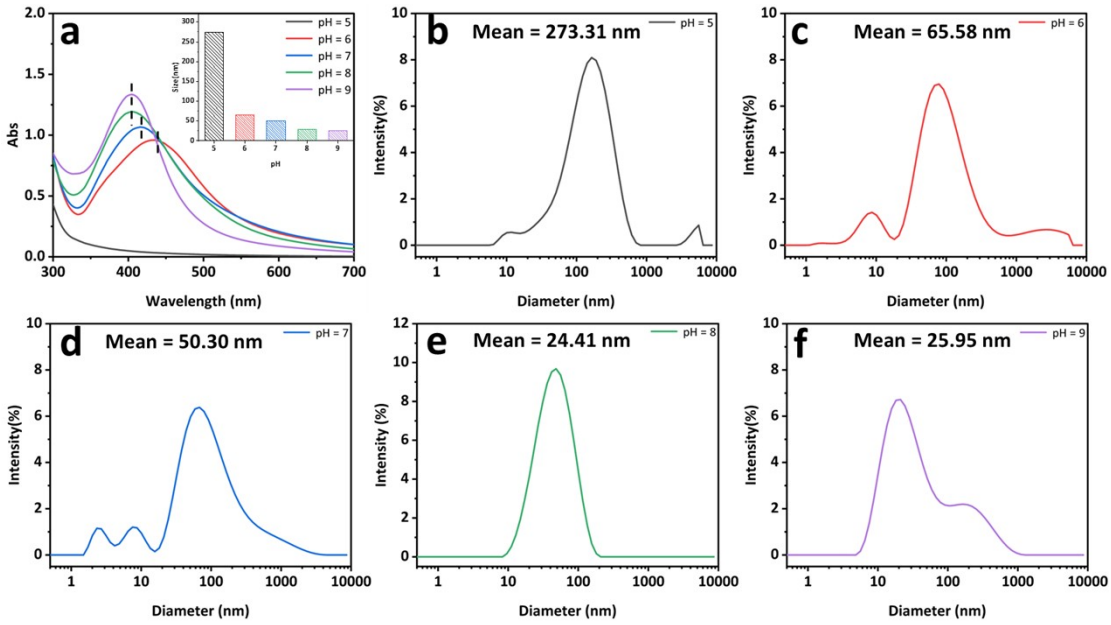

Fig. S2 (a) UV-vis spectra (Inset: average particle size diagram) and (b-f) DLS curves of BD-CQDs@AgNPs solution prepared under different pH conditions.

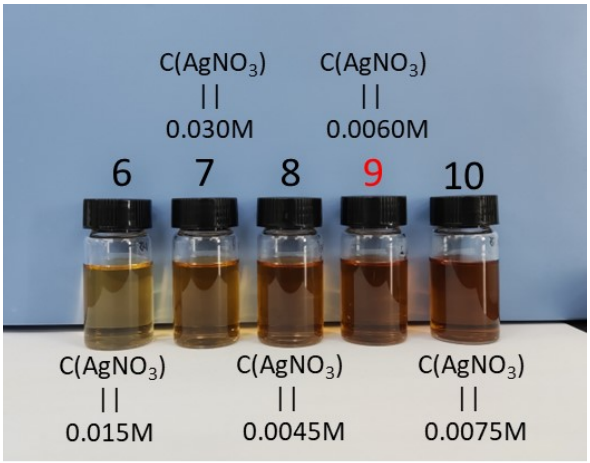

212

213 **Fig. S3** Photos of BD-CQDs@AgNPs solutions prepared under different concentrations of $AgNO_3$.

214

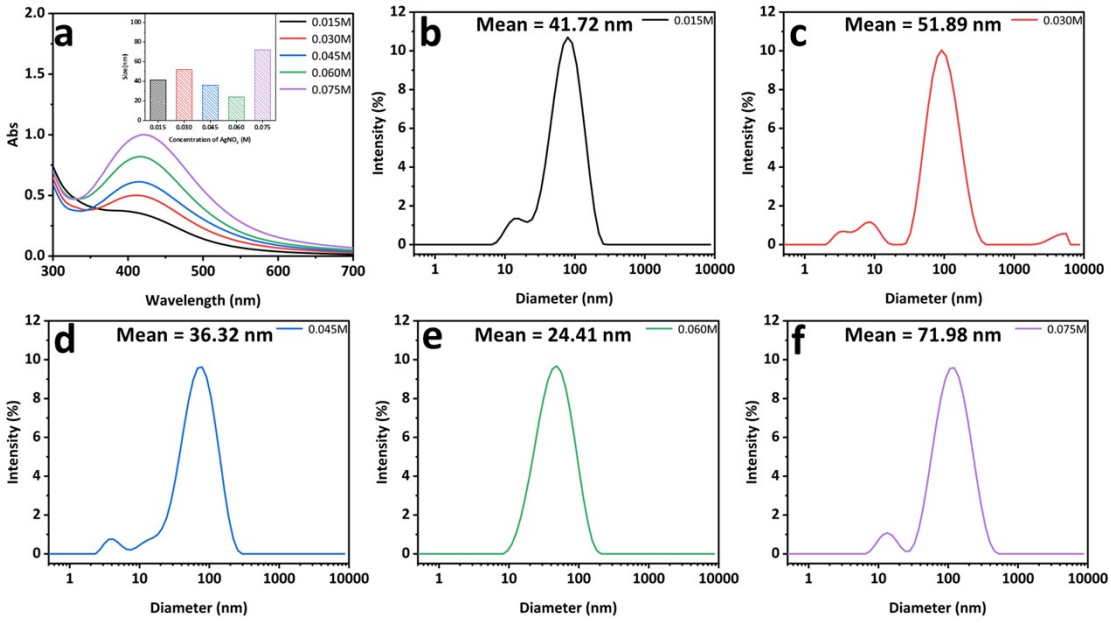

215

216 **Fig. S4** (a) UV-vis spectra (Inset: average particle size diagram) and (b-f) DLS curves of BD-

217 CQDs@AgNPs solution prepared under different concentrations of $AgNO_3$.

218

219

220

221

222

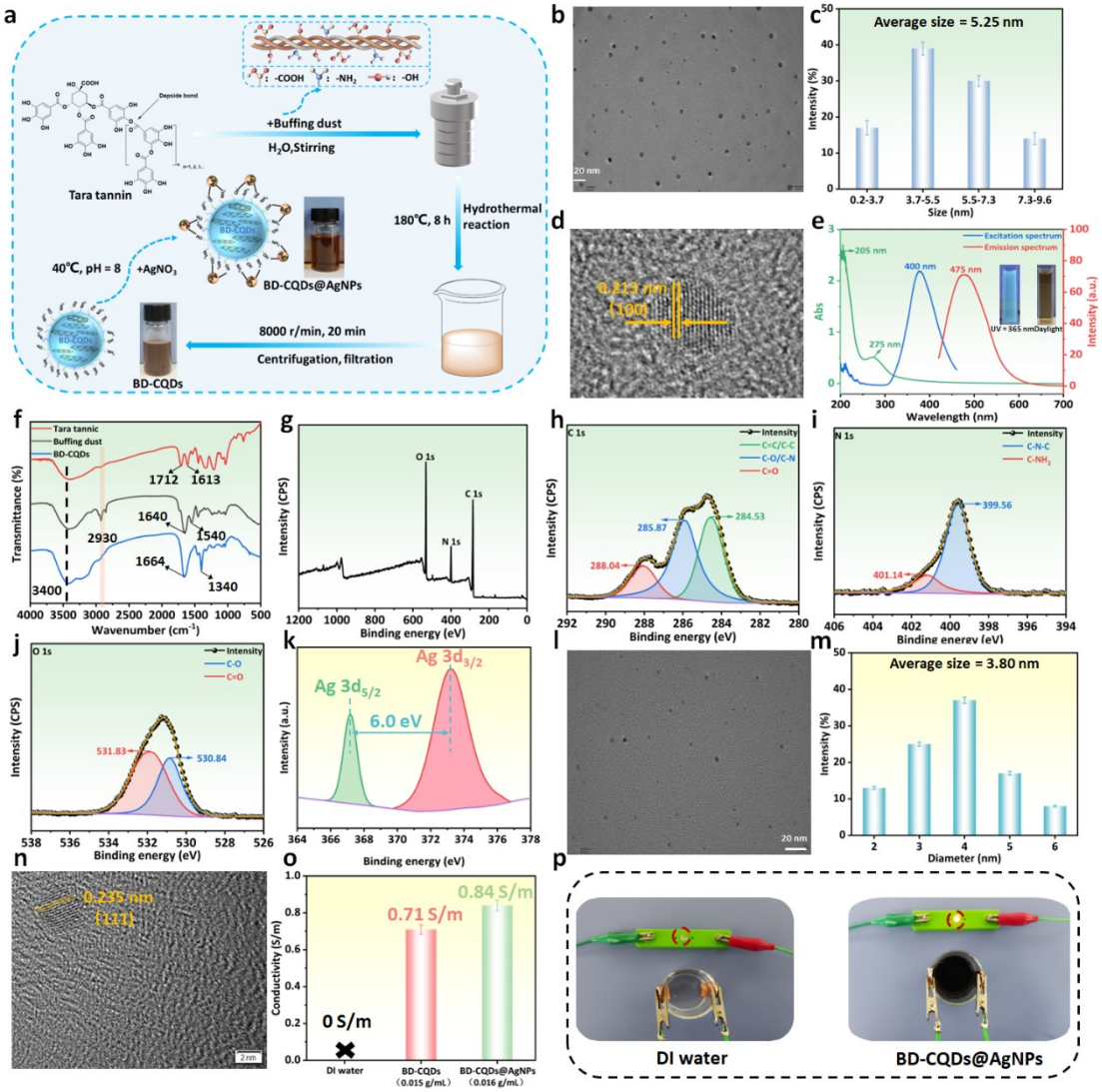

Fig. S5 Preparation and characterization of BD-CQDs and CQDs@AgNPs. (a) Schematic illustration of the preparation of BD-CQDs and BD-CQDs@AgNPs. TEM image (b), particle size distribution (c), and HR-TEM image (d) of BD-CQDs. (e) UV-vis spectrum, excitation spectrum (blue line) and emission spectrum (red line) of BD-CQDs (Inset: photos of the BD-CQDs solutions under a 365 nm UV lamp (left) and daylight (right). (f) FTIR spectra of Tara tannin, BD and BD-CQDs. (g) XPS spectra of BD-CQDs. High-resolution C 1s (h), N 1s (i) and O 1s (j) spectra of BD-CQDs. (k). High-resolution Ag 3d spectrum of BD-CQDs@AgNPs. TEM image (l), particle size distribution (m), and HR-TEM image (n) of BD-CQDs@AgNPs. (o) Conductivity of BD-CQDs and BD-CQDs@AgNPs solutions. (p) Brightness comparison of LED lamp in DI water and the BD-CQDs@AgNPs solution.

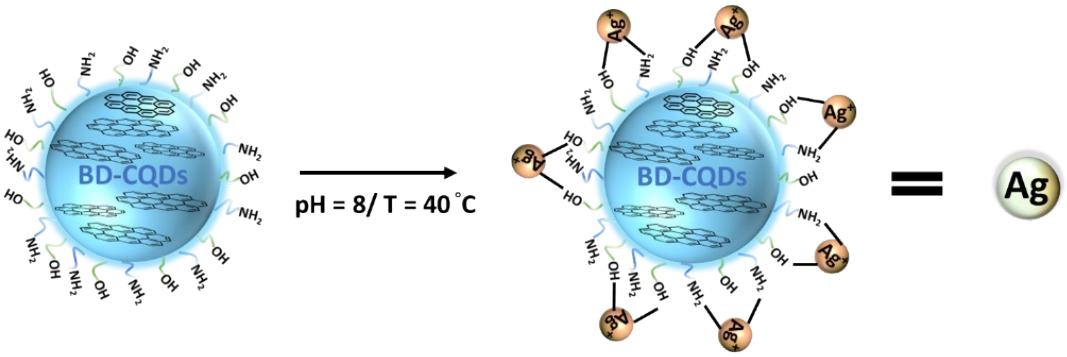

235

236 **Fig. S6** Synthesis schematic diagram of BD-CQDs@AgNPs.

237

238

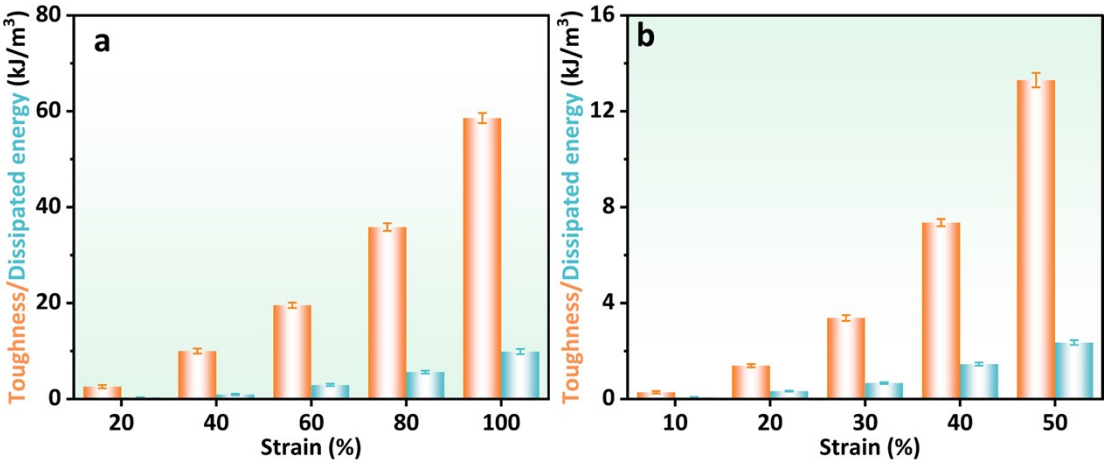

239

240 **Fig. S7** Toughness and dissipated energies of the tensile loading-unloading cycles (a) and the

241 compression loading-unloading cycles (b) of BPGC-Gly at different stains.

242

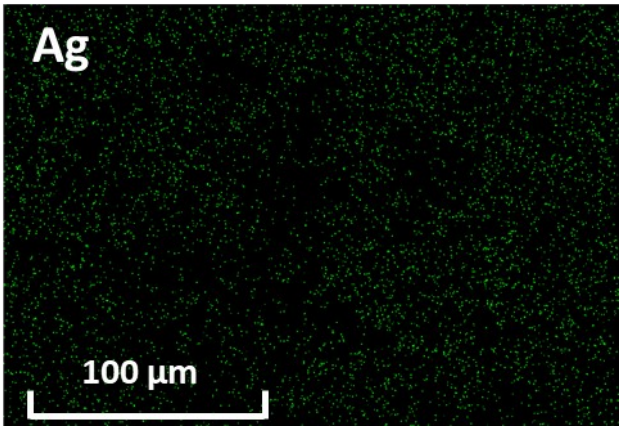

243

244 **Fig. S8** EDS mapping image of Ag elements in the BPGC-Gly.

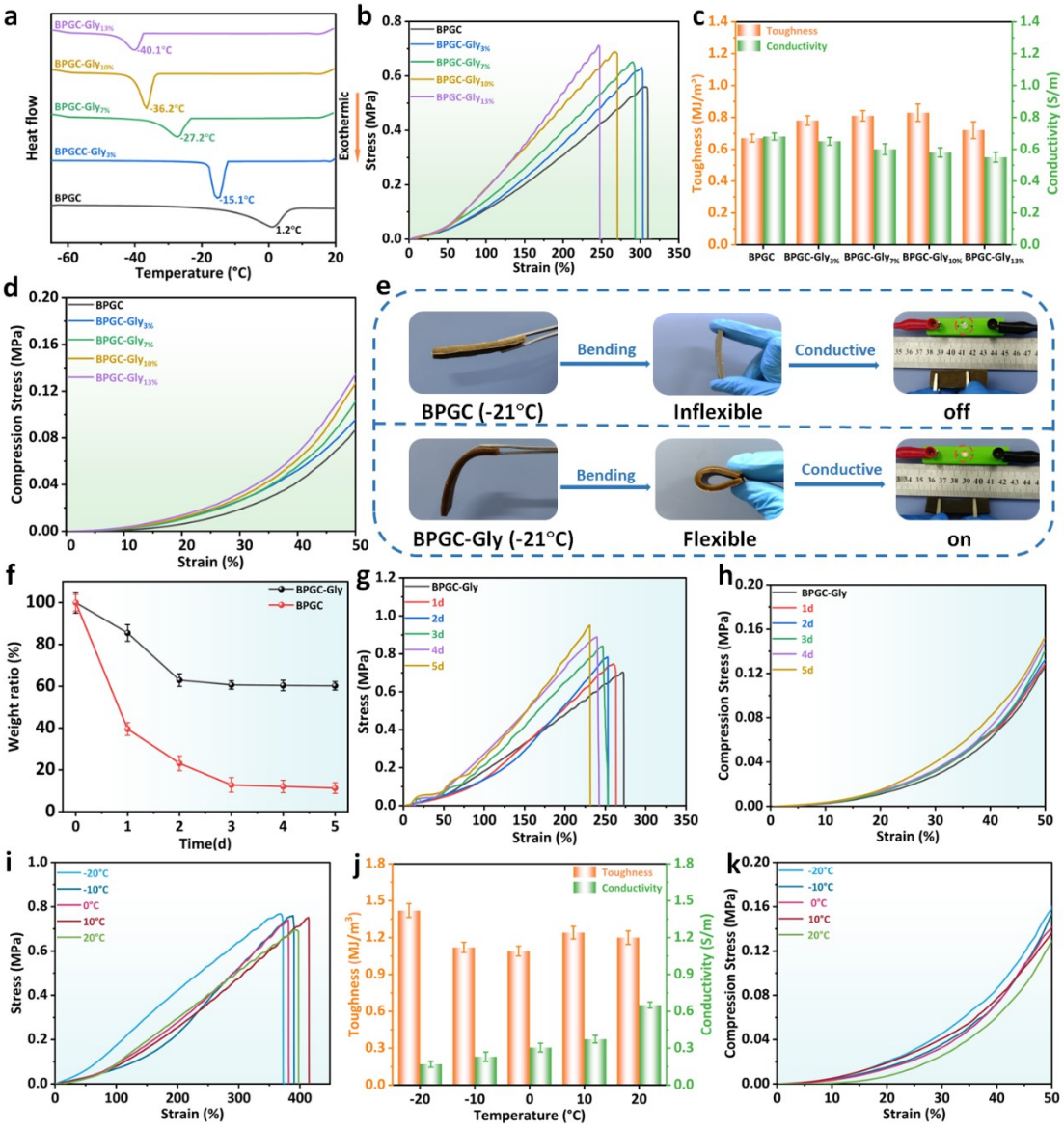

Fig. S9 Anti-freezing and moisturizing properties of BPGC-Gly. DSC curves (a), stress-strain curves (b), tensile toughness and conductivity (c), and compression stress-strain curves (d) of BPGC-Gly hydrogels with different Gly contents. e) Pictures of anti-freezing and lighting up LEDs for BPGC and BPGC-Gly at -21°C. f) Moisturizing curves of BPGC and BPGC-Gly after 5 days of placement. Stress-strain curves (g) and compression stress-strain curves (h) of BPGC-Gly after 5 days of placement. Stress-strain curves (i), tensile toughness and conductivity (j), and compression stress-strain curves (k) of BPGC-Gly under different environments.

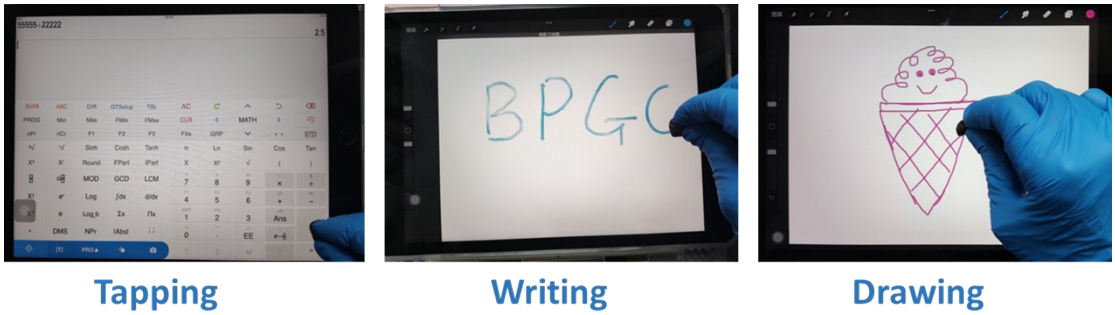

Fig. S10 Tapping, writing and drawing patterns on the iPad screen using BPGC hydrogel as a stylus.

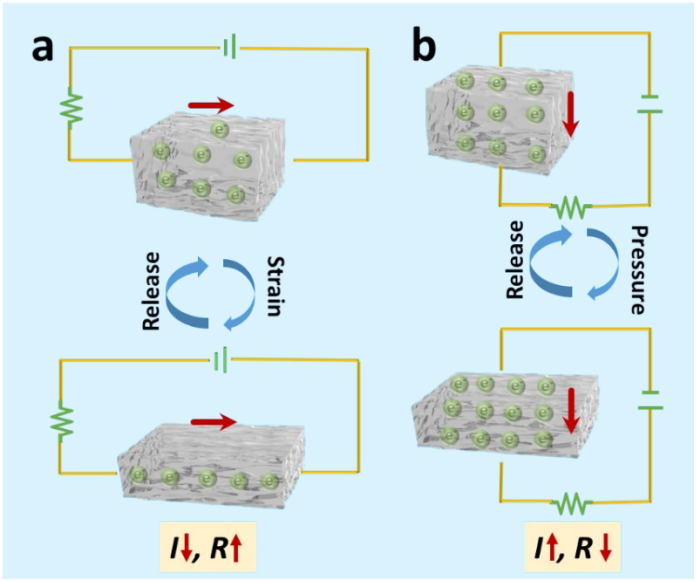

Fig. S11 Schematic diagram of the BPGC-Gly strain (a) and pressure sensors (b).

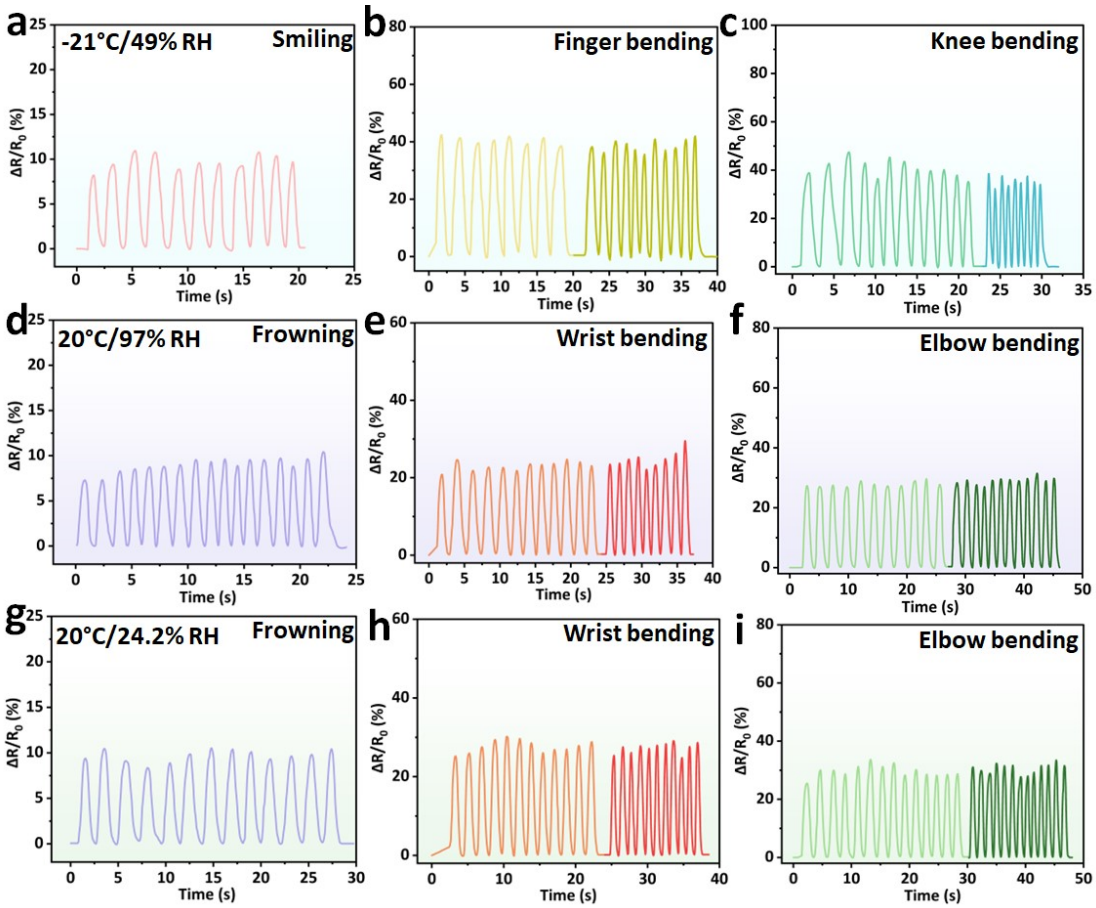

Fig. S12 Real-time $\Delta R/R_0$ change curves of BPGC-Gly strain sensors under different motions (smiling(a), finger bending(b), knee bending(c)) after 60 h of placement at -21 °C with 49% RH. Real-time $\Delta R/R_0$ change curves of BPGC-Gly strain sensors under different motions (frowning (d), wrist bending (e), elbow bending (f)) after 60 h of placement at 20 °C with 97% RH. Real-time $\Delta R/R_0$ change curves of BPGC-Gly strain sensors under different motions (frowning (g), wrist bending (h), elbow bending (i)) after 60 h of placement at 20°C with 24.2% RH.

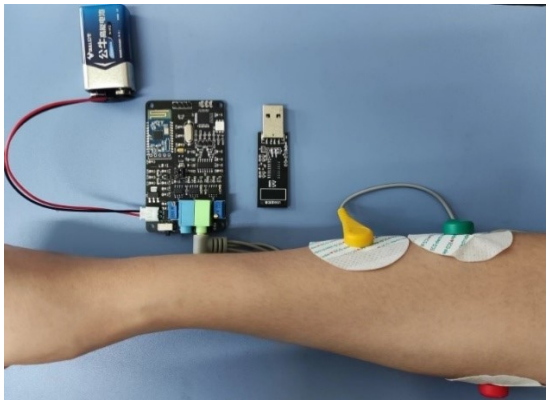

Fig. S13 Schematic diagram of bioelectrical signal device wearing

Table S1. Main components, PDI and Zeta potential of BD-CQDs@AgNPs prepared at different pH conditions

Sample	CQDs (mL)	$AgNO_3$ (0.06M, mL)	pH	T (°C)	PDI	Zeta potential (mV)
1	5	0.2	5	40	0.447	-12.2
2	5	0.2	6	40	0.552	-32.1
3	5	0.2	7	40	0.535	-31.6
4	5	0.2	8	40	0.277	-39.2
5	5	0.2	9	40	0.418	-25.1

Table S2. Main components, PDI and Zeta potential of BD-CQDs@AgNPs prepared at different concentrations of $AgNO_3$.

Sample	CQDs (mL)	$AgNO_3$ (mL)	pH	T (°C)	PDI	Zeta potential (mV)
6	5	0.2 (0.015M)	8	40	0.291	-23.6
7	5	0.2 (0.030M)	8	40	0.421	-29.1
8	5	0.2 (0.045M)	8	40	0.316	-33.3

9	5	0.2 (0.060M)	8	40	0.277	-39.2
10	5	0.2 (0.075M)	8	40	0.308	-32.1

Table S3. Comparison of sensing type, pressure sensitivity, working range and conductivity of hydrogel pressure sensors.

Hydrogel network	Sensing type	Pressure sensitivity	Working range	Conductivity (S/m^{-1})	Ref
ACC/PAA/alginate	Capacitance	0.17 kPa^{-1}	1 kPa	-	S14
SA/NaCl/PAM	Resistance	1.45 kPa^{-1}(0-1.5 kPa) 0.02 kPa^{-1}(1.5-100 kPa)	100 kPa	0.01	S15
DCMC/AG/PAA	Resistance	3.92 kPa^{-1} (0–6.9 kPa) 0.016 kPa^{-1} (6.9–100 kPa)	100 kPa	3.6	S16
PEG/Na_2SO_4	Resistance	0.006 kPa^{-1}	-	0.238	S17
OVA/PAM/Fe^{3+}	Resistance	2.9 kPa^{-1}(0 - 4 kPa) 1.66 kPa^{-1}(4 - 100 kPa) 0.57 kPa^{-1} (100 - 320 kPa)	320 kPa	-	S18
PVA/CNTs/graphene	Resistance	0.127 kPa^{-1}(0 - 5 kPa) 0.041 kPa^{-1}(5 - 10 kPa)	10 kPa	-	S19
PVA/AA	Resistance	0.841 kPa^{-1} (0 - 3 kPa) 0.446 kPa^{-1} (3 - 10 kPa) 0.074 kPa^{-1} (10 - 30 kPa)	30 kPa	-	S20
PDA@CNT/PAM	Resistance	4.16 kPa^{-1} (0 -7.9 kPa)	15kPa	-	S21
PAA/CNC-g-P(VAm-co-AM)	Resistance	0.0183 kPa^{-1}(0 - 75 kPa) 0.003kPa^{-1} (75 - 150kPa)	150 kPa	0.123	S22
BD/PVA/Gel/CQDs	Resistance	4.26 kPa^{-1} (0 – 12.5 kPa) 0.86 kPa^{-1} (12.5 – 55.5 kPa) 0.18 kPa^{-1} (55.5 - 125 kPa)		0.70	This work

"-": indicates no mention in the literature

Table S4. Comprehensive performance comparison of BPGC-Gly with previously reported multifunctional hydrogels.

Sample	Tensile Stress	Tensile strain	Conductivity (S/m)	GF	S (kPa^{-1})	Multimodal monitoring types	Ref
CPAL	1.11 MPa	2472%	1.09	2.99	-	3	9
PVA/NaCl-P	1.60 MPa	550%	-	-	-	1	12
PSDM/TWS	-	-	-	-	37.04	3	23
NSD-Gel	7.33 MPa	263.1%	-	-	-	3	33
PAA/LA-Ag/MXene	0.30 MPa	400%	-	9.17	0.33	2	36
PCOBE	2.15 MPa	880%	7.34	7.0	-	2	37
Starch/PAA	0.060 MPa	135%	-	0.98	1.57	4	49
DMAEA/AA	0.48 MPa	1880%	-	15.41	0.032	3	55
BPGC-Gly	0.72 MPa	270%	0.70	1.33	4.26	5	This work

"-": Indicates no mention in the paper.

References

S1 J. Shen, Z. He, J. W. Zhang, H. Guo, W. Lin and H. B. Gu, *Polymer*, 2023, **288**, 126471.

S2 Z. He, J. C. Liu, X. Fan, B. Song and H. B. Gu, *Ind. Eng. Chem. Res.*, 2022, **61**, 17915–17929.

S3 I.-A. Baragau, N. P. Power, D. J. Morgan, R. A. Lobo, C. S. Roberts, M.-M. Titirici, V. Middelkoop, A. Diaz, S. Dunn and S. Kellici, *ACS Sustain. Chem. Eng.*, 2021, **9**, 2559–2569.

S4 W. Ulfat, A. Mohyuddin, M. Amjad, M. H. D. Othman, P. Gikas and T. A. Kurniawan, *J. Environ. Manag.*, 2023, **347**, 119129.

S5 K. M. Qi, Y. P. Ye, B. Wei, M. X. Li, Y. X. Lun, X. Y. Xie and H. J. Xie, *J. Hazard. Mater.*, 2022, **432**, 128759.

S6 Z. He, J. Shen, J. Zhang, W. Lin and H. Gu, *ACS Sustain. Chem. Eng.*, 2023, **11(35)**, 13126–13141.

S7 K. Patchai Murugan, S. Sabarinathan, N. Prabhakaran and S. Swarnalatha, *Chem. Eng. J.*, 2023, **468**, 143547.

S8 J. Liu, F. Zhang, Z. An, W. Shi and H. Li, *RSC Adv.*, 2021, **11(44)**, 27183–27192.

S9 J. C. Liu, X. Fan, D. Astruc and H. B. Gu, *Collagen & Leather*, 2023, **5(1)**, 17.

S10 X. Yao, S. Zhang, L. Qian, N. Wei, V. Nica, S. Coseri and F. Han, *Adv. Funct. Mater.*, 2022, **32**, 2204565.

S11 H. Haidari, R. Bright, X. L. Strudwick, S. Garg, K. Vasilev, A. J. Cowin and Z. Kopecki, *Acta Biomater.*, 2021, **128**, 420–434.

S12 J. Y. Yang, Y. Chen, L. Zhao, Z. P. Feng, K. L. Peng, A. L. Wei, Y. L. Wang, Z. R. Tong and B. Cheng, *Compos. Pt. B-Eng.*, 2020, **197**, 108139.

S13 J. L. Lopez-Miranda, M. A. Vázquez González, F. Mares-Briones, J. A. Cervantes-Chávez, R. Esparza, G. Rosas and R. Pérez, *Res. Chem. Intermed.*, 2018, **44**, 7479–7490.

S14 Z. Lei, Q. Wang, S. Sun, W. Zhu, P. Wu, Adv. Mater. 2017, **29 (22)**, 1700321.

S15 X. Zhang, N. Sheng, L. Wang, Y. Tan, C. Liu, Y. Xia, Z. Nie, K. Sui, Materials Horizons 2019, **6 (2)**, 326-333.

S16 Q. Ling, T. Ke, W. Liu, Z. Ren, L. Zhao, H. Gu, Ind. Eng. Chem. Res. 2021, 60 (50), 18373-18383.

S17 S. Zhao, P. Tseng, J. Grasman, Y. Wang, W. Li, B. Napier, B. Yavuz, Y. Chen, L. Howell, J. Rincon, F. G. Omenetto, D. L. Kaplan, Adv. Mater. 2018, **30 (25)**, 1800598.

S18 A. Zheng, Y. Qin, Q. Xia, X. Zhang, Y. Chen, ACS Applied Polymer Materials 2023, **5 (4)**, 2312-2322.

S19 Y. Zhang, E. Ren, A. Li, C. Cui, R. Guo, H. Tang, H. Xiao, M. Zhou, W. Qin, X. Wang, L. Liu, Journal of Materials Chemistry B 2021, **9 (3)**, 719-730.

S20 L. Zhou, Q. Xin, J. Lin, S. Liang, G. Yang, Applied Materials Today 2023, **34**, 101907.

S21 W. He, X. Guo, P. Xia, S. Lu, Y. Zhang, H. Fan, J. Colloid Interface Sci. 2023, **647**, 456-466.

S22 B. Li, Y. Chen, W. Wu, X. Cao, Z. Luo, Carbohydr. Polym. 2023, **317**, 121092.